Forecasting the *Dst* index during corotating interaction region events using synthesized solar wind parameters

T. Andriyas,[1] E. Spencer,[1] A. Raj,[1] J. Sojka,[2] and M. L. Mays[3]

Received 20 July 2011; revised 14 December 2011; accepted 29 December 2011; published XX Month 2012.

[1] Observations from SOHO, STEREO, and ACE during the declining phase of the solar cycle toward the deep minimum in 2008 are analyzed to establish the timing of corotating interaction region (CIR) activity. This analysis is then employed to synthesize signals of the *z* component of the interplanetary magnetic field (IMF) B_z, solar wind radial velocity v_x, and solar wind proton density N_p at 1 AU. The synthesized signals are used as a substitute for ACE measurements to represent solar wind forcing due to coronal hole driven CIR events occurring during multiple Bartel rotations (BR 2381 to BR 2393). The signals drive a low-order physics-based model of the magnetosphere called WINDMI, one of whose outputs is the ground-based measurement of the *Dst* index. Estimating the arrival of CIR events for future rotations using ACE and SOHO data during BR 2381 produced what we refer to as an uncalibrated yearly forecast. We next generated a video-calibrated estimate of the arrival times of CIR events in addition to information from BR 2381 using SOHO and STEREO images of the Sun in order to produce a simulated 3.5 day ahead forecast of possible geomagnetic activity. The time of arrival of CIR events is taken to be the travel time of density compressions as seen in a noninertial frame according to a radial solar wind speed of 500 km/s and a distance of 1 AU. We were able to forecast the timing of CIR-induced geomagnetic activity to within 12 h for 17 out of 28 events by using the expected recurrence of the events through multiple Bartel rotations together with SOHO and STEREO coronal hole sightings made 3.5 days before every event. The uncertainty in the IMF B_z led to a forecast of levels of geomagnetic activity on an ensemble basis, yielding a distribution of different possible *Dst* signatures. We used a 10-sample ensemble and a 50-sample ensemble to obtain typical representations of geomagnetic activity. Depending on the periodicity and intensity of fluctuations in B_z, we obtained higher or lower levels of activity and shorter or longer times for the recovery of the *Dst* to quiet levels.

Citation: Andriyas, T., E. Spencer, A. Raj, J. Sojka, and M. L. Mays (2012), Forecasting the *Dst* index during corotating interaction region events using synthesized solar wind parameters, *J. Geophys. Res.*, *117*, AXXXXX, doi:10.1029/2011JA017018.

1. Introduction

[2] Solar wind properties are closely associated with the phase of solar cycle. During solar maximum, the solar wind carries transient bursty events like coronal mass ejections (CMEs) while during a minimum, most of interplanetary space is filled with recurrent fast and slow solar wind sectors [*Zhang et al.*, 2008; *Richardson et al.*, 2000]. It is well known that the fast solar wind emanates from open field lines with foot points in coronal holes [*Nolte et al.*, 1976; *Gosling and Pizzo*, 1999]. The fast wind is quite stable with speeds ranging from 650 to 800 km/s [*McComas et al.*, 2002]. At or close to maximum, the coronal holes mainly occupy the high latitudes around the poles with most of the low latitudes covered with active regions. During the declining phase of the solar cycle, these holes can extend to latitudes close to the ecliptic plane [*Burlaga et al.*, 1978] owing to interchange reconnection with closed field lines of the neighboring active regions [*Edmondson et al.*, 2010].

[3] As a consequence of spatial variability in the coronal expansion and solar rotation, solar wind flows of different speeds become radially aligned [*Gosling and Pizzo*, 1999]. Compressive interaction regions are produced when high-speed streams catch up with slower plasmas [*Schwenn*, 1990]. When the flow pattern is roughly time stationary, these compression regions form spirals in the solar equatorial plane that corotate with the Sun. These regions are called corotating interaction regions (CIRs).

[4] Within a CIR region, the magnetized plasma is compressed and therefore amplifies the magnetic field fluctuations [*Tsurutani et al.*, 1995]. These fluctuations are nonlinear ($\delta\mathbf{B}/\mathbf{B} \approx 1$–$2$) and cause mild geomagnetic storms (Dst ≥ -100 nT) with long recovery times which can last for one solar rotation (≈27 days). Since the geoeffectiveness

[1] Center for Space Engineering, Utah State University, Logan, Utah, USA.
[2] Center for Atmospheric and Space Sciences, Utah State University, Logan, Utah, USA.
[3] NASA Goddard Space Flight Center, Greenbelt, Maryland, USA.

0148-0227/12/2011JA017018

of solar wind structures are related closely to the amplitude of the *z* component (B_z) of the interplanetary magnetic field (IMF), any southward turning of the magnetic field component B_z in the GSM coordinate system leads to the onset of a geomagnetic storm when a CIR disturbance arrives at 1 AU. The recovery from geomagnetic activity due to a CIR is delayed by the Alfvenic fluctuations and turbulence in the high-speed stream (HSS) following the CIR [*Turner et al.*, 2006], leading to considerable amounts of energy being transferred into the magnetosphere. Although the energy input into the magnetosphere during an interplanetary CME (ICME) is larger than during a CIR event, the average energy over the solar minimum can be greater than during solar maximum [*Sheeley et al.*, 1977; *Tsurutani et al.*, 1995].

[5] CIR events have been studied from both theoretical and simulation perspectives. *Carovillano and Siscoe* [1969] derived the solar wind parameters at 1 AU on the basis of a hydrodynamic approximation with an assumed source surface velocity perturbation. *Siscoe and Finley* [1970, 1972] extended this work to include asymmetry and arbitrary perturbations. *Lee* [2000] derived the solar wind flow parameters by considering the evolution of forward and backward traveling pressure waves into shocks which generally form after 1 AU. Three dimensional simulations were done by *Pizzo* [1980] to see the evolution of a hydrodynamic stream between a source surface and 1 AU and to study the fast stream slow stream interaction in greater detail. *Pizzo* [1991] also simulated the CIR evolution with an MHD formulation and examined the effect of tilted dipole fronts. Recently, *McGregor et al.* [2011] used the ENLIL-WSA model to study the interaction of fast and slow streams in order to interpret the composition measured at 1 AU.

[6] CIRs are the main sources of geomagnetic storms during solar minimum. These storms have weak main phases but prolonged recovery phases because of rapid Alfvenic fluctuations inside the HSS. The solar wind magnetosphere coupling occurs mainly through flux transfer events leading to weak injection of particles into the ring current and hence weak geoeffectiveness. Apart from the Alfvenic fluctuations, the magnetic field also has another feature which can affect the dynamics of the magnetosphere. Magnetic holes (MH) and magnetic decreases (MD) [*Turner et al.*, 1977] are pressure balance structures that are found interspersed with CIR events. *Tsurutani et al.* [2002] indicate that such decreases are due to perpendicular particle acceleration by the ponderomotive force on phase steepened edges of Alfven waves. The heated particles decrease the total magnetic field through the diamagnetic effect. Since the total magnetic field decreases (or magnetic pressure reduces), the plasma beta (ratio of thermal to magnetic pressure) increases and so does the number density. These density or dynamic pressure enhancements compress the magnetopause.

[7] Inside the magnetosphere and the magnetotail, relativistic electrons are also detected during the passage of a HSS. Ultralow frequency (ULF) oscillations which are frequencies that range between 1 mHz to 1 Hz [*Jacobs et al.*, 1964] (i.e., from the lowest-order mode that a magnetospheric cavity can support up to various ion gyro frequencies) in the Pc5 (2–7 mHz) range [*O'Brien et al.*, 2001; *Mann et al.*, 2004] and resonant interaction of cyclotron with electromagnetic chorus [*Meredith et al.*, 2003] have been theorized as the acceleration mechanisms behind these electrons.

[8] To build a forecasting model using the fact that coronal holes are sources of fast winds, *Robbins et al.* [2006] used solar images from the Kitt peak telescope to determine the size and location of coronal holes to have a 8.5 day ahead prediction of solar wind velocity (included period of maxima). *Luo et al.* [2008] used the brightness of the SOHO/EIT 28.4 nm wavelength images to create a new forecasting parameter and correlated it to the solar wind speed. *Vrsnak et al.* [2007a, 2007b] calculated the fractional coronal hole area in a longitudinal slice and related it to solar wind parameters and *Dst* index measured on ground. Solar wind parameters (v_r, $|B|$, N_p) were calculated on the basis of time offsets after the alignment of a coronal hole in the central meridian slice ($-10°$ to $10°$) in the GOES X-ray (SXI) images.

[9] In this work, we construct a set of synthetic signals to estimate the solar wind parameters measured at 1 AU (the location of ACE) on the basis of the detection of coronal holes in SOHO images (EIT 19.5 nm wavelength). The synthetic signals are fed to the Solar Wind–Magnetosphere–Ionosphere (WINDMI) model which produces a sample forecast *Dst* signal which is compared against actual *Dst* measured on the ground and also against the *Dst* that would be produced if the actual satellite data were used as input into the model. The model is available for runs on request at the Community Coordinated Modeling Center (CCMC) Web site (http://ccmc.gsfc.nasa.gov/models/modelinfo.php?model=WINDMI). The motivation was not only to test the forecasting capability of the WINDMI model, but also to constrain the ring current energy levels during CIR events for later comparison against CME driven events. We also wanted to examine the role and importance of each solar wind parameter in the development of CIR driven storms.

[10] This paper is organized as follows. Section 2 describes the sources of data and images along with the models and CME prediction software used to examine the events. Section 3 provides a brief summary of previous works which were used to construct the synthetic flow parameters (v_x, B_z, N_p) to replace the ACE parameters. Section 4 explains the WINDMI model that is used to forecast the geoeffectiveness of the simulated storms by examining the *Dst* profiles against measured ground *Dst*. In section 5, the results from pre and post video calibration is discussed and some issues regarding the forecasting process are highlighted in section 6. The paper ends with a summary of the work done and possible future work in section 7.

2. CIR Data

[11] The period under investigation was the year 2008 corresponding to Bartel rotations (BR) 2381–2393. During the early part of 2008, there were two coronal holes extending toward lower latitudes leading to alternate high- and slow-speed winds in the ecliptic plane in a four sector structure [*Carovillano and Siscoe*, 1969]. This is part of a period of an extended solar minimum from 2006 to 2009 [*de Toma*, 2010]. Because of low CME activity, a structured solar wind, and the presence of coronal holes near the ecliptic [*de Toma*, 2010], this period was well suited for the study of CIR events. Following a 1.3 year periodicity [*Richardson et al.*, 1994], the mean solar wind speed also reduced from 500 km/s to around 350 km/s toward the end of 2008.

[12] We used solar wind data from the Advanced Composition Explorer (ACE) satellite located at the L1 point between the Sun and the Earth. Measurements from the Solar Wind Parameters (SWEPAM) instrument were used for solar wind velocity v_x and proton density N_p while the Interplanetary Magnetic Field Parameters (MAG) instrument gave IMF B_z. Hourly averaged data was used for all three parameters. Whenever corrupted data points were encountered, they were replaced by their previous values. We used the hourly averaged data over each 27 day solar rotation period called the Bartel rotation. SOHO 19.5 nm images from the Extreme ultraviolet Imaging Telescope (EIT) from the Solar Weather Browser (SWB) were used for the sighting of coronal holes. The SWB is an image analyzing tool developed by the Royal Observatory of Belgium which includes a database of images from in situ and ground-based observations. These images can be overlaid with spherical grids along with detected active regions provided by NOAA or CME source regions. STEREO B satellite images from the Sun Earth Connection Coronal and Heliospheric Investigation (SECCHI) instrument's Extreme Ultraviolet Imager (EUVI; 19.5 nm wavelength) were used in the absence of SOHO data. STEREO A was not chosen for coronal hole images since it was located ahead of the Earth (≈21° to ≈43°) during the period of analysis. According to the Parker spiral, a CIR would already have been detected at ACE (1 AU) by the time a coronal hole was seen at STEREO A.

[13] Synoptic maps of photosphere and subearth location relative to the heliospheric current sheet were examined to determine the current sheet crossings by ACE. The maps are provided at the CCMC STEREO support Web site (http://ccmc.gsfc.nasa.gov/stereo support.php). Fast flows and CMEs during the year were checked using the Computer Aided CME Tracking (CACTus) [*Robbrecht and Berghmans*, 2004] software available on http://sidc.oma.be/cactus/ along with in situ particle and field signatures as mentioned by *Zurbuchen and Richardson* [2006].

[14] The magnetospheric response to solar wind disturbances is measured by the *Dst*, *AL*, *AU*, and *sym-H* indices. For comparison against the synthetic *Dst* produced by the WINDMI model, we used the *Dst* index. It is based on average values of the horizontal component of the Earth's low-latitude magnetic field. Hourly values of the measured *Dst* were taken from the World Data Center for Geomagnetism (WDC) Kyoto Web site (http://wdc.kugi.kyoto-u.ac.jp/).

3. Synthetic Signal Profiles

[15] Since the coronal holes are sources of the fast solar wind, the number of equatorial coronal holes will determine the fast and slow wind sector structure in the solar ecliptic plane. A four sector structure corresponds to two periods of fast and two periods of slow wind in the velocity profile. Using this correspondence, we created a radial flow velocity profile.

[16] The fast variations were superimposed on a 1.3 year cycle, as found by *Richardson et al.* [1994], and a slower 11 year trend due to the solar activity cycle. *Carovillano and Siscoe* [1969] solved for the plasma parameters that would be measured at 1 AU using a hydrodynamic formulation without latitudinal dependence. The solutions were found by using a sinusoidally varying profile for radial and azimuthal velocity along with density. They found that the calculated peak in density lead the peak in radial velocity by a phase of $\pi/2$. This implied that the density reached a maximum on the rising edge of the radial velocity. Compressions occur when the fast wind catches up with the slow wind which also leads to compressions of the magnetic field. Sector crossings accompany the transition from slow to fast wind.

[17] The density enhancements (heliospheric current sheet crossings) are directly correlated to the arrival time of the CIR stream interface at 1 AU. With the solar wind propagation speed taken as 500 km/s, we calculated an approximate travel time of 3.5 days from the solar surface to 1 AU. We subtracted 3.5 days from the ACE satellite time of density enhancements to identify the coronal holes in SOHO/EIT images for BR 2381. These coronal holes were then used as a reference. To simulate density enhancements, we used the technique of *Wood et al.* [2010] to model the compression as a Gaussian pulse. The width of the Gaussian pulse was determined from data during BR 2381. The amplitudes were sinusoidally modulated with a 1.3 year variation.

[18] The IMF B_z was generated on the basis of a 60–68 min Alfvenic fluctuation [*Hviuzova et al.*, 2007], superposed on a normally distributed random signal based on the work by *Padhye et al.* [2001]. A mean field strength of 2 nT was assumed. For the amplification of the magnetic field perturbations in the CIR, proton density Gaussian profiles and bandwidths were used to modulate the magnetic field profile, but the compressions were delayed by 1 day as statistically found by *Vrsnak et al.* [2007a].

[19] In sections 3.1–3.3, we separately employ two schemes to time the density compressions since it was found that the density compressions measured at ACE occurred at slightly different times during different rotations. The two schemes were termed "uncalibrated" and "video calibrated." The uncalibrated results were generated by using the density enhancement timings from BR 2381 repeated throughout the year as shown in Figure 1. These timings were based on a fixed periodicity of occurrence of each CIR event, assuming the flow structures to be stationary in the Sun's rotating frame. In section 5.1, we apply a correction to the assumed periodic appearance of a coronal hole using images of coronal holes seen during each rotation during 2008. If a coronal hole was sighted earlier than the usual periodicity indicated, we moved the density compression back in time to compensate for the discrepancy. We moved a density compression forward if the coronal hole was sighted later. We refer to these corrected timings as the video-calibrated results.

3.1. Radial Velocity Profile

[20] The velocity profile is based on a faster 14 day variation superimposed on a slower 40 day variation. The two periods are the sum and difference of 13 and 27 days (roughly a half and a full Bartel rotation). The mean solar wind speed is chosen as 500 km/s. Apart from these shorter time variations, longer variations based on a 1.3 year solar cycle and the 11 year solar cycle are also added. The amplitudes of the profiles are chosen to be approximately the solar wind speeds observed during the first rotation. The profile is written as

$$v_x = v_{mean} + v_2 \cos\theta_4 + v_3 |\sin\theta_3| + v_4[\cos(\theta_1 - \theta_2) + \cos(\theta_1 + \theta_2)], \quad (1)$$

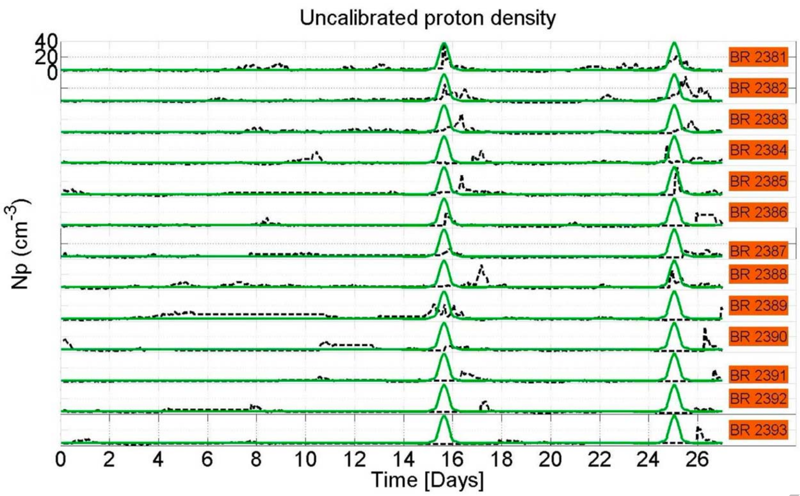

Figure 1. The measured solar wind proton density time series from ACE (dashed black line) and the synthetic solar wind proton density (solid green line) assuming a periodic repetition starting in BR 2381.

where v_{mean} = 500 km/s, $\theta_1 = \omega_1 t$, $\theta_2 = \omega_2 t$, $\theta_3 = \omega_3 t$, $\theta_4 = \omega_4 t$, and $\omega_1 = 2\pi/T_1$, $\omega_2 = 2\pi/T_2$, $\omega_3 = 2\pi/T_3$, and $\omega_4 = 2\pi/T_4$ with periods T_1 = 13 days, T_2 = 27 days, T_3 = 1.3 years, and T_4 = 11 years, respectively. Here the coefficients v_2 = 100 km/s, v_3 = 5 km/s, and v_4 = 50 km/s are estimated by analyzing the velocity data during BR 2381.

3.2. Proton Density Profile

[21] The density profile is generated on the basis of the satellite data for the first rotation. Similar to *Wood et al.* [2010], we assume that a CIR compression region is a Gaussian shaped wave as seen by HI instrument on board STEREO A and B [*Wood et al.*, 2010]. The width of the Gaussian is chosen to correspond to the width of the density enhancements that appear in the first rotation. The amplitude of the Gaussian profile was modulated with a cosine function with a 1.3 year variation. The density profile is given by

$$N_p = N_{mean} + a\left[U(t-T_i^n)e^{-\frac{(t-T_i^n)^2}{2\sigma^2}}\right]\cos\theta_n, \qquad (2)$$

where N_{mean} is the mean proton density of 3 cm^{-3} and a is the amplitude of density enhancement in the compression regions, taken to be 50 cm^{-3} on the basis of looking at first rotation, $\theta_n = \omega_n{}^t$, T_i^n is the day when the i^{th} coronal hole aligned with the central meridian (0°) in the SOHO image time advanced by 3.5 days to account for propagation of the disturbance to 1 AU, $U(t - T_i^n)$ is a box function to account for a time limited Gaussian pulse, width of pulse $\sigma \approx 1$ day centered at T_i^n, and ω_n corresponds to a 1.3 year period.

[22] The arrival time T_i^n of the proton density compressions is on days 15.6 and 25 of BR 2381 for the uncalibrated signal as shown in Figure 1 (i.e., $T_i^n = 15.6$ and $T_2^n = 25$ in the synthetic density profile). These timings were then used throughout the year to generate an uncalibrated synthetic density profile (Figure 1).

[23] In the video-calibrated scheme, the arrival times were corrected on the basis of the appearance of coronal holes using SOHO and STEREO B images. Between BR 2381 to BR 2393, STEREO B was located ≈24°–31° west (at a distance of 0.4–0.6 AU, in heliocentric Earth ecliptic (HEE) coordinates) of the Earth and the density compression arrivals were corrected accordingly using the same propagation speed of 500 km/s.

3.3. North-South Magnetic Field Profile

[24] *Dungey* [1961] pointed out that geomagnetic activity is strongly correlated to the north-south component of the interplanetary magnetic field (IMF). Fluctuations in IMF B_z therefore play a significant part in driving geomagnetic storms. Producing the IMF B_z signal is key to accurately forecasting the CIR driven storm.

[25] Because of processes near the solar surface and flow interactions in interplanetary space, the IMF B_z has turbulent Alfvenic fluctuations around 68 min [*Hviuzova et al.*, 2007]. These Alfvenic fluctuations are also normally distributed [*Padhye et al.*, 2001]. In the compression region (velocity transition from slow to fast), these fluctuations are amplified in the same way as the density signal. Moderate *Dst* values during such storms indicate that energy input during the main phase of the storm is low. Also, following the compression in the HSS, the IMF B_z periodically turns southward which causes a delayed *Dst* recovery. This may precondition the magnetosphere before the next storm onset [*Richardson et al.*, 2006].

[26] We construct IMF B_z as a random fluctuation modulated by a Gaussian profile that occurs during every density enhancement,

$$B_z = p\left[B_{mean} + B_{amp}U(t-T_i^b)e^{-\frac{(t-T_i^b)^2}{2\sigma^2}}\right]\cos\theta_b, \qquad (3)$$

where θ_b is the Alfvenic period of 68 min [*Hviuzova et al.*, 2007], p is a randomly generated number chosen from a normal distribution with values between 0 and 1 over a length of time t, and B_{mean} and B_{amp} are the mean field and perturbed amplitudes (2 and 7 nT, respectively). The time shifts T_i^b are the days when a coronal hole was seen in the SOHO image advanced by 3.5 days (propagation time of the disturbance to 1 AU) with an additional 1 day according to *Vrsnak et al.*

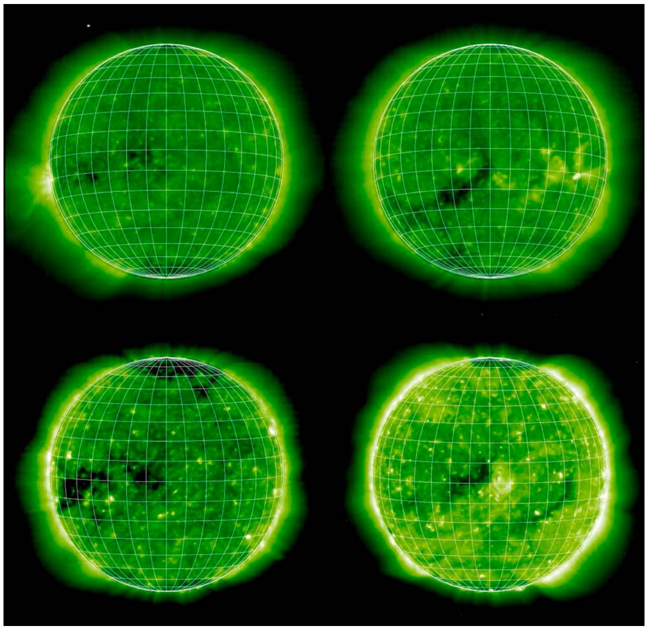

Figure 2. SOHO Extreme ultraviolet Imaging Telescope (EIT) and STEREO B Extreme Ultraviolet Imager ((EUVI) bottom right) images taken in 19.4 nm wavelength that were used for timing the synthetic compressions at 1 AU. (top) The two reference coronal holes observed during BR 2381. (bottom) The coronal holes during BR 2387 that was used in the video calibration process. The start time for CIR travel is determined to be when the leading edge is aligned with the central meridian.

[2007a] (i.e., $T_i^b = T_i^n + 1$), and $U(t - T_i^b)$ being a box function and σ the width as before.

4. WINDMI Model of the Magnetosphere

[27] The plasma physics–based WINDMI model uses the solar wind dynamo voltage, V_{sw}, generated by a particular solar wind–magnetosphere coupling function to drive eight ordinary differential equations describing the transfer of power through the geomagnetic tail, the ionosphere and the ring current.

[28] The major current systems that are considered to contribute to the total *Dst* in the magnetosphere are (1) the magnetopause currents shielding Earth's dipolar magnetic field, (2) the symmetric ring current, (3) the partial ring current, and (4) the cross-tail current along with the closure currents on the magnetopause. All these currents cause magnetic perturbations on the Earth's surface.

[29] The model is available on the CCMC Web site. The output of the model are the *AL* and *Dst* indices. The simulated *Dst* index is given by

$$Dst = Dst_{rc} + Dst_{mp} + Dst_t, \tag{4}$$

where Dst_{mp} is the perturbation due to the magnetopause currents, Dst_t is the magnetic field contribution from the tail current and Dst_{rc} is the magnetic field due to the ring current. The contributions from the magnetopause and tail current systems are given by

$$Dst_{mp} = a\sqrt{P_{dyn}}, \tag{5}$$

$$Dst_t = \alpha I(t). \tag{6}$$

The tail current $I(t)$ is modeled by WINDMI as I, the geotail lobe current in the northern hemisphere. P_{dyn} is the dynamic pressure exerted by the solar wind on the Earth's magnetopause. For Dst_{mp} and Dst_t in nT, a and α are defined in units of nT nPa$^{-1/2}$ and nT A^{-1}. In this work we used the WINDMI model with nominal physical parameters. We refer the reader to *Patra et al.* [2011] for values of a, α, and other details of the model.

[30] The solar wind dynamo voltage V_{Bs} used to drive the model is generated using the Rectified IMF Driver [*Reiff and Luhmann*, 1986] coupling function ($E_{sw} = vB_s$) which is modified to give

$$V_{Bs} = 40(kV) + v_{sw}B_sL_y^{eff}(kV), \tag{7}$$

where v_{sw} is the x-directed component of the solar wind velocity in GSM coordinates, B_s is the southward IMF component and L_y^{eff} is the effective cross tail width over which the dynamo voltage is produced. For northward or zero IMF Bz, a base viscous voltage of 40 kV is used to drive the system. The rectified $v_{sw}B_s$ was preferred over other coupling functions as it has been shown to be a more robust driver compared to other coupling functions, while maintaining reasonably good feature reproduction capability [*Spencer et al.*, 2007]. Since we use the rectified $v_{sw}B_s$ driver, seasonal and dipole tilt effects are not taken into account in the analysis.

[31] The Dst_{rc} signal is obtained from the plasma energy stored in the ring current W_{rc} calculated by the WINDMI model. It is given by the Dessler-Parker-Sckopke (DPS) relation [*Dessler and Parker*, 1959; *Sckopke*, 1966]

$$Dst_{rc} = \frac{\mu_0 W_{RC}(t)}{2\pi B_E R_E^3}, \tag{8}$$

where B_E is the Earth's surface magnetic field along the equator. The ring current energy in the model is assumed to be lost by particles drifting out of orbit or by charge exchange processes at a rate proportional to τ_{rc}.

5. Results

[32] Solar wind plasma and magnetic field data measured by ACE satellite located upstream of the Earth at L1 point were used to ascertain the arrival times of CIR disturbance. With an average solar wind speed of 500 km/s, the travel time for the disturbance is approximately 3.5 days. After subtracting 3.5 days from the time of measurement of a particular CIR compression, we obtained the images shown in Figure 2 (top) for BR 2381. The leading edge of the equatorial coronal hole was aligned very well with the central meridian in a $-10°$ to $0°$ longitude slice. Note that later during the video calibration stage we start the propagation of CIR transients

Table 1. Timing of Density Compressions Before Video Calibration[a]

BR	T_1^n	T_2^n	ME
2381	0	0	N
2382	0	+	N
2383	+	+	N
2384	+	–	Y
2385	+	+	N
2386	0	+	Y
2387	0	+	N
2388	+	0	N
2389	0	+	N
2390	0	+	N
2391	+	+	N
2392	+	+	Y
2393	+	+	Y

[a]Codes and abbreviations are as follows: 0, arrival of a synthetically generated disturbance on time; +, arrival of a disturbance before detection by ACE; −, arrival after detection by ACE; BR, Bartel rotation; ME, missed event.

for every rotation when the leading edge of a coronal hole is aligned with the central meridian.

[33] Table 1 summarizes the timings of the disturbances before video calibration was done. In Table 1, a plus sign indicates that the recurrent CIR transient measured at ACE occurred later than expected from the alignment procedure. A minus sign indicates that the CIR transient measured at ACE occurred earlier than expected. We also mention that the missed events (ME) noted in Table 1 are events that appear in the ACE measurements but are not accounted for in the expected recurrence of coronal holes. We expected this to improve when video calibration was performed, as will be discussed in section 5.1.

[34] As seen in Figure 1, the CIRs arrived at 1 AU on day 15.6 and day 25 for the first rotation. These compressions were a result of fast streams emanating from the coronal holes seen 3.5 days earlier (Figure 2, top) that caught up with the slow stream ahead. Using the timings of compression from the first rotation, a synthetic proton density was generated for the whole year using equation 3.2. The resulting profile is shown in Figure 1. As seen in Figure 1, the difference between the simulated and measured arrival times varied from 0.5 to 1.7 days with variable compression amplitudes and widths over the remaining rotations.

[35] Radial IMF (B_x(GSE)) polarity changed from negative (Southern coronal hole) to positive (Northern coronal hole) during the first compression and then back again to negative during the next (25th day) compression, which indicated that we were indeed looking at the right coronal holes. ACE data was then replaced with synthetic profiles of the proton density and the IMF B_z. Using the WINDMI model, we then produced a forecast of geomagnetic activity for the year by repeating the occurrence of the density and IMF B_z enhancements. Figure 1 also shows that a third compression happened on day 10 of BR 2384 which occurred intermittently in the following rotations. Apart from these, there were instances when a compression happened in both the proton density and magnetic field but the velocity profile did not show an increase. Since these were not classical CIR signatures, we did not consider them as events. We found that the compression in B_z was delayed by a day as given by *Vrsnak et al.* [2007a] with respect to the density enhancements owing to compression and subsequent current sheet crossings.

[36] The forecasted *Dst* is shown in Figure 3. A quick look at Figure 4 (which is the same as Figure 3 but plotted for the whole of 2008) shows that the timings of these storms is captured to within −12 to +12 h. However, the main phase is overemphasized in many instances going down to as low as −100 nT when the ground *Dst* was only around −70 nT at most. This is in part due to the Dst_{mp} which is directly related to the density enhancement, while the storm main phase is more related to IMF B_z (equation (4)). Any error in timing may result in a large error in the forecasted *Dst*. Sometimes the amplitudes in the *Dst* profile are overemphasized because of the random nature of B_z and a higher simulated compared to measured value of N_p.

[37] In section 5.1, using SOHO and STEREO images, we determined the time for CIR propagation as starting when the leading edge of the coronal hole is aligned with the central

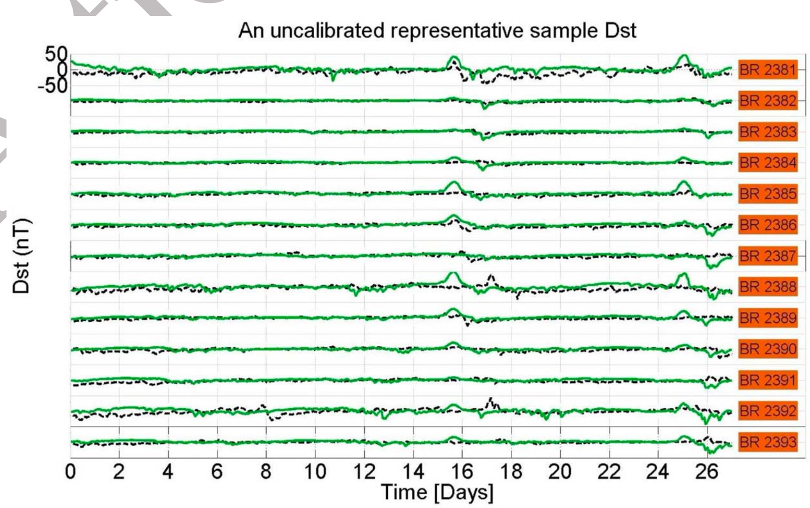

Figure 3. Measured *Dst* index (dashed black line) compared to a synthetic *Dst* index (solid green line) with assumed periodic repetition of compressions, prior to video calibration. Note that this represents one of many possibilities depending on the B_z signal.

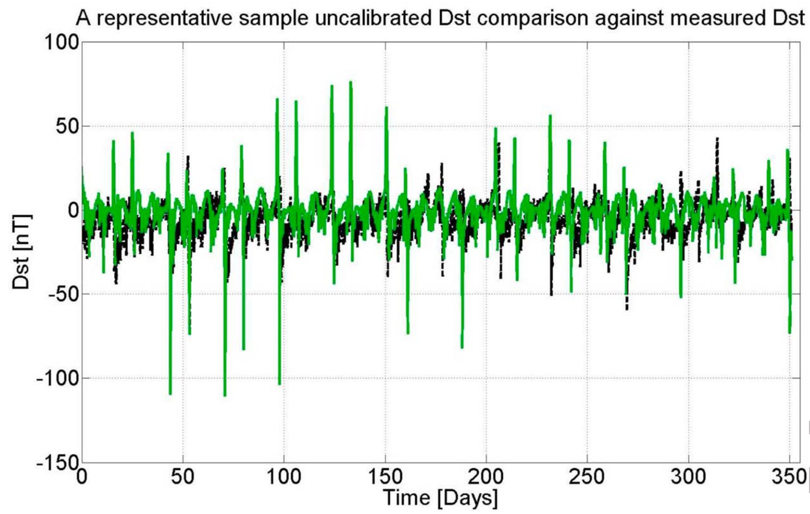

Figure 4. Yearly measured *Dst* (dashed black line) compared to synthetic *Dst* (solid green line) data with assumed periodic repetition of compressions.

meridian. Figure 2 (bottom) shows sample images from BR 2387 to illustrate the procedure.

5.1. Video-Calibrated Timing

[38] To correct the arrival time at 1 AU, the timing of the density compressions was deduced using images from the Extreme Ultraviolet Imaging Telescope (EIT 19.5 nm) on board the SOHO satellite found on SWB. We apply a correction to the assumed periodic appearance of a coronal hole using images of coronal holes seen during each rotation during 2008. If a coronal hole was sighted earlier than the usual periodicity indicated, we moved the density compression back in time to compensate for the discrepancy. We moved a density compression forward if the coronal hole was sighted later. This video-calibrated synthetic signal was used to forecast a three day advanced *Dst*.

[39] When a coronal hole is detected, we advance the video to the instant t_{ref}^{VC} in time when the leading edge of the hole boundary coincides with the central meridian of the Sun, which is directly aligned with the SOHO and ACE spacecraft at L1. We then use the average velocity of the solar wind to calculate the time when a CIR event will be detected at ACE if it begins propagating out at t_{ref}^{VC}. This information is then used to correct the assumed periodic arrival time of CIR events at L1 that was produced with the uncalibrated scheme.

[40] Using this method, we found that for the year, coronal holes in the $-10°$ to $0°$ longitude and $-30°$ to $30°$ latitude slice correlated well with the compression regions at 1 AU. Figure 5 shows the density profile for the thirteen rotations using the images to time the arrival of a CIR disturbance at 1 AU. Table 2 shows the result of using solar images to time the compression arrivals at 1 AU.

[41] There are instances (e.g., the second compression in BR 2383) when there was a coronal hole but it did not produce a CIR. In addition, there were some missed events for example on day 26 of BR 2387 and BR 2388. The missed CIRs (e.g., in BR 2387) were added from the uncalibrated signal assuming that the coronal holes were stable. These

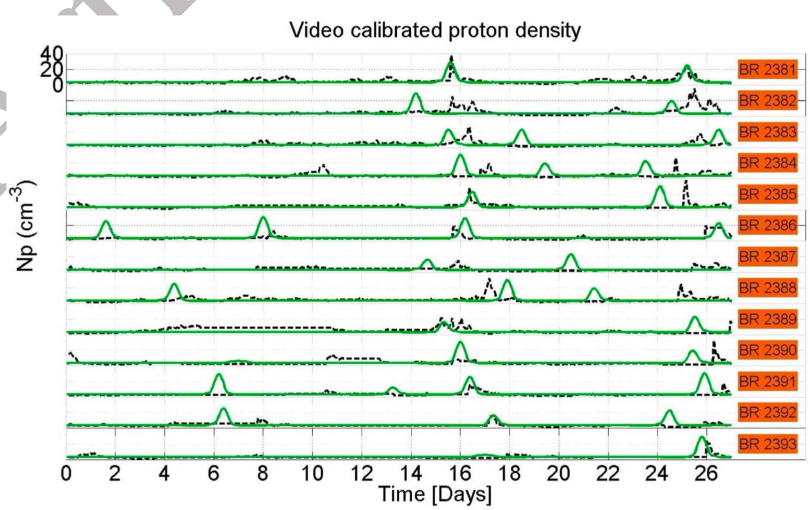

Figure 5. Proton density measured by ACE (dashed black line) compared to synthetic proton density (solid green line) after video-corrected arrival times at 1 AU.

Table 2. Timing of Density Compressions After Video Calibration[a]

BR	T_1^n	T_2^n	T_3^n	T_4^n
2381	0	0	n/a	n/a
2382	+	+	n/a	n/a
2383	+	FA	–	n/a
2384	ME	+	FA	+
2385	0	+	n/a	n/a
2386	FA	+	–	0
2387	+	FA	ME	n/a
2388	FA	–	FA	ME
2389	0	+	n/a	n/a
2390	FA	0	+	n/a
2391	FA	FA	0	+
2392	+	0	+	n/a
2393	ME	+	+	n/a

[a]FA stands for false alarm, and n/a indicates not applicable. Other notation is as in Table 1.

added compressions appear in blue in the density plots of BR 2387 and 2388 in Figure 6. We added these compressions although they do not appear in the images to emphasize that the assumed periodicity and stability of coronal holes can sometimes help with the forecast. There are also false alarms mentioned in Table 2 that were checked in the ENLIL runs provided on the CCMC Web site.

[42] Figure 6 is a summary plot of proton density. We used STEREO B for timing when images from SOHO were unavailable due to CCD bakeout. This is shown in magenta in Figure 6. We found two compressions during BR 2383 and BR 2388 that arrived earlier than expected. The reason for the early arrival times are not clear. The *Dst* output from the WINDMI model is shown in Figure 7.

6. Discussion

[43] Since the storm onset is related to the polarity of IMF B_z, the quality of the forecast depends on how good an estimate of B_z we can generate. The signal is turbulent with amplifications occurring inside the compression region. Some ambiguity exists as to the time when B_z turns southward owing to the signal being random. Therefore, the onset of the storm as seen in the "simulated *Dst*" (Figure 3) will be delayed or advanced accordingly even if the two compressions, either in satellite or synthetic data, occurred at the same time. The negative peak of the "synthetic *Dst*" can be over or underemphasized owing to the signal being a random number multiplied by B_{amp}. The magnetopause current contribution comes from Dst_{mp} and it depends directly on the dynamic pressure and in turn on proton density. Since $Dst_{mp} \geq 0$, it pushes the *Dst* to positive values. Therefore, any simulated compressions that do not show up in the ACE data, will nevertheless raise the simulated *Dst* curve. Twenty-six out of the 30 CIR events were forecasted within a time span of −12 to +12 h of occurrence of the peak of the measured *Dst* for each event during the uncalibrated analysis.

[44] The false alarms (FA) in Table 2 occur when coronal holes were seen but there was no disturbance registered at ACE. To cross-check these events, synoptic maps from CCMC's STEREO support page were examined for any current sheet crossings. We discuss this further for each rotation in sections 6.1–6.13.

[45] Knowing that the amplification of B_z occurs inside the CIR, which in turn occurs approximately a day after the density enhancement [*Vrsnak et al.*, 2007a], we needed to carefully analyze the quality of the synthetic *Dst* during each event. The randomness of B_z caused the main phase peak of the simulated storm to occur at times different from the data. Therefore, we proceeded to obtain an average of the simulated *Dst* from WINDMI over 10 representative samples and also of 50 representative samples (to see if the timings are consistent in terms of being forecasted before or after being measured as compared with 10 representative samples). This was compared against the timing of the storm time negative peaks in the ground *Dst*.

[46] In the next few subsections, we discuss each storm to assess the quality of the forecasts after video calibration. Table 3 represents a summary of the timings for 10 and 50 representative samples compared against ground *Dst*. The samples are called representative since they represent one out of many possible outcomes from a normally distributed

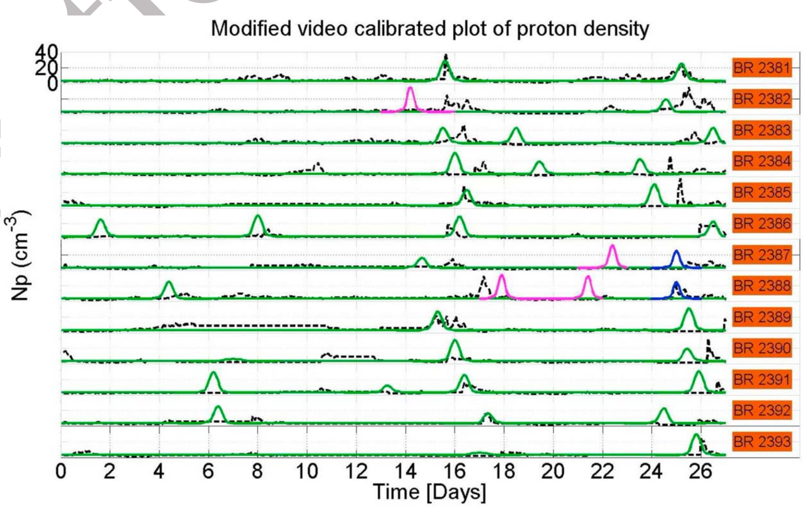

Figure 6. Plot of modified video-corrected proton density profile with ACE data (dashed black line), synthetic signal (solid green line), uncalibrated periodic density compressions (blue line), and coronal holes sighted by STEREO B (magenta line).

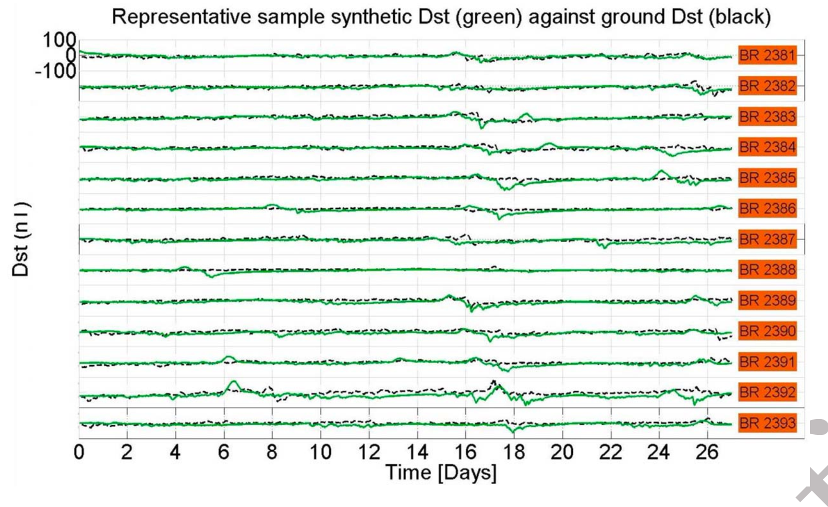

Figure 7. A representative sample *Dst* output from WINDMI (solid green line) after video corrections compared to *Dst* from ground measurements (dashed black line).

Table 3. *Dst* Timing and Peak Negative Amplitude Comparison Against Ground *Dst* After Averaging 10 and 50 Representative Samples of Synthetic *Dst*

		Dst_{avg} for 10 Samples		Dst_{avg} for 50 Samples		DSt_{grd}
Bartel Rotation	Storm[a]	Timing	Magnitude (nT)	Timing	Magnitude (nT)	Magnitude (nT)
2381	1	+	−30	+	−34	−44
	2	−	−23	−	−21	−28
2382	3	+	−33	+	−34	−45
	4	+	−40	+	−38	−72
	5	+	−54	+	−62	−43
2383		FA	n/a	n/a	n/a	n/a
	6	−	−20	−	−18	−29
		ME				−19
	7	+	−50	+	−39	−43
2384		FA	n/a	n/a	n/a	n/a
	8	+	−36	+	−36	−22
2385	9	+	−41	+	−39	−33
	10	+	−68	+	−58	−20
		FA	n/a	n/a	n/a	n/a
2386	11	−	−62	−	−41	−16
	12	−	−58	−	−61	−40
	13	−	−19	−	−18	−25
	14	+	−28	+	−32	−40
2387		FA	n/a	n/a	n/a	n/a
	15	ME(+)	−28	ME(+)	−25	−24
		FA	n/a	n/a	n/a	n/a
2388	16	−	−30	−	−28	−40
		FA	n/a	n/a	n/a	n/a
	17	ME(+)	−35	ME(+)	−33	−26
2389	18	−	−35	−	−46	−51
	19	+	−15	+	−17	−29
		FA	n/a	n/a	n/a	n/a
2390	20	+	−41	+	−38	−37
	21	+	−22	+	−20	−60
		FA	n/a	n/a	n/a	n/a
		FA	n/a	n/a	n/a	n/a
2391	22	−	−50	−	−45	−24
	23	+	−22	+	−21	−30
	24	+	−11	+	−19	−31
2392	25	−	−55	−	−52	−11
	26	+	−33	+	−31	−32
		ME				−18
2393	27	+	−41	+	−37	−15
	28	−	−16	−	−16	−14

[a]See Figure 8.

randomly generated IMF B_z. We also give a short account of the compressions that occurred during each Bartel rotation, whether or not they were correctly captured through our forecasting technique, and whether the forecasted timing was before or after the measured timing. The word "forecasting" used in the description should be understood to mean that we analyzed SOHO and STEREO B image data during every Bartel rotation, identified coronal holes in the images at particular times, and then used the timing information to generate synthetic signals of CIR disturbances that would be measured at 1 AU 3.5 days later.

[47] We refer to measured data as the actual data recorded by the ACE spacecraft and ground-based *Dst* index stations.

[48] For reference, if we mention a code 0, this means an event that was forecasted and measured to occur at roughly the same time. If we mention a code +, this means the event was forecasted to occur at a particular time but actually occurred later according to ACE. If we mention a code –, this means the event was forecasted to occur at a particular time but actually occurred earlier according to ACE. The code FA indicates a false alarm, and the code ME indicates a missed event. These codes also appear in Table 2.

6.1. BR 2381 (Starting 16 January 2008)

[49] The density compressions during the first rotation were timed using the ACE satellite data. Because the compressions during this rotation were used as reference, each was forecasted accurately. This can be seen by the 0 in Tables 1 and 2.

[50] The amplified IMF B_z in the compression region caused the measured *Dst* index to reach a storm time peak of −44 nT on day 17 (00:00 UT) of BR 2381. In contrast, for a 10-sample ensemble average, the simulated *Dst* storm peak occurred around 22:00 UT of day 16. The peak happened around 21:00 UT of day 16 for the 50 sample ensemble average.

[51] During the second storm, the HSS solar wind speed peaked to around 700 km/s with the IMF reaching a peak value of approximately 20 nT. The measured *Dst* peaked to −28 nT on 00:00 UT of day 26. This storm peaked at 08:00 UT of day 26 for a 10-sample ensemble average. With a 50 sample ensemble average, the simulated *Dst* peaked on 23:59 UT of day 26.

6.2. BR 2382 (Starting 12 February 2008)

[52] The first compression in density was measured around 00:00 UT of day 16 but was forecasted to happen earlier as seen in Table 2. The compressions in IMF B_z which followed the plasma compression caused the measured *Dst* to peak around 23:00 UT of day 16. With a 10-sample ensemble average, the simulated *Dst* peaked at 11:00 UT of day 15. This was also the case with the 50-sample ensemble average which peaked an hour later, around 12:00 UT of day 15.

[53] The second density compression that preceded the storm was strong with density values peaking to 40 particles cm^{-3}. The strong compression was accounted for by a very large positive *Dst* of 32 nT. The storm peak *Dst* had a value of −72 nT on 06:00 UT of day 26. With the 10-sample ensemble average, the simulated peak storm time was found at 15:00 UT of day 25. The timing got closer to the measured peak time for the 50-sample ensemble average with a negative maximum occurring around19:00 UT of day 25.

6.3. BR 2383 (Starting 10 March 2008)

[54] The first storm was measured on 22:00 UT of day 17 with a peak *Dst* of −43 nT. It was forecasted to happen earlier as shown in Table 2. With the 10-sample ensemble average, the peak storm simulated *Dst* was timed around 19:00 UT of day 16. With the 50-sample ensemble average the peak occurred at 20:00 UT of day 16.

[55] A second storm was measured on 07:00 UT of the first day of BR 2384 on the ground. The delay caused in timing the density compression caused the simulated storm peak to occur around 22:00 UT of day 3 of BR 2384 for the 10-sample ensemble average. The simulated storm peak was forecasted to be at 20:00 UT of day 3 of BR 2384 for the 50-sample ensemble average.

[56] As seen in Table 2, between these two storm events, another compression was forecasted which was a false alarm (FA). The coronal hole seen in the SOHO images did not produce any transients at ACE.

6.4. BR 2384 (Starting 6 April 2008)

[57] The first storm in this rotation had a typical CIR signature with compressions occurring ahead of the HSS (with a speed peaking to around 600 km/s). As seen in Figure 6, a compression happened on 11:00 UT of day 10. No coronal holes were seen in the EIT images so this event was considered a missed event (ME) in Table 2.

[58] The second compression was forecasted before it was measured at ACE as seen in Table 2. The IMF B_z enhancement that followed the proton density compression resulted in a geomagnetic storm that peaked to a minimum of −43 nT around 19:00 UT of day 17. With the 10-sample ensemble average, the simulated storm peak occurred on 06:00 UT of day 17. With the 50-sample ensemble average, the peak occurred on 07:00 UT of day 17.

[59] The last storm was measured with a peak *Dst* of −22 nT on 15:00 UT of the day 26. This event was consistently forecasted before the actual ground measurement as seen in Figure 8 (event 8 on the x axis). With the 10-sample ensemble average, the simulated *Dst* peaked on 21:00 UT of day 24. With the 50-sample ensemble average, the peak occurred on 19:00 UT of day 24.

[60] Table 2 indicates that a third compression was forecasted between the two CIR storms. This compression was a FA because the fast stream that emanated from the coronal hole seen in SOHO/EIT 194 nm images produced no disturbance at ACE.

6.5. BR 2385 (Starting 3 May 2008)

[61] Table 2 indicates that two coronal holes were observed and that two associated CIR compressions were measured by ACE.

[62] The first storm is event 9 in Table 3 and Figure 8. This storm was forecasted on time with regard to the proton density enhancement (see Table 2). The measured *Dst* peaked to a value of −33 nT around 05:00 UT of day 18. The simulated *Dst* from both the 10- and 50-sample ensemble averages was forecasted earlier than when it was measured. For the 10-sample ensemble, the storm peak occurred on 21:00 UT of day 17. The storm peaked on 17:00 UT of day 17 for the 50-sample ensemble average. This result is due to the randomness in the IMF B_z signal because the first amplified

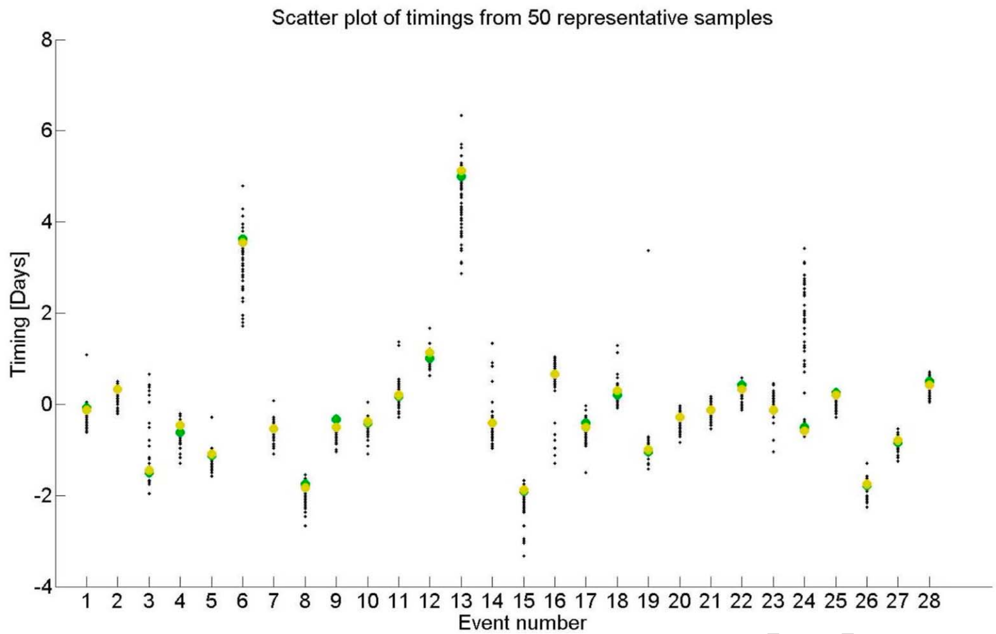

Figure 8. Scatterplot of the times when the *Dst* samples peaked to storm time values compared to peaks in the measured *Dst*. The 0 on the y axis indicates that the forecasted peak coincides with the measured peak. The 10-sample average is indicated with solid green circles, and the 50-sample average is shown with yellow circles.

southward turning can occur anywhere inside the compression region.

[63] The second CIR had a strong compression with a measured value of approximately 40 particles cm^{-3} on the rising edge of solar wind speed which transitioned from around 350 km/s to a HSS of 600 km/s. This storm was forecasted earlier but measured later by ACE. The storm induced by this CIR was only weakly geoeffective with a measured peak magnitude of −20 nT on 18:00 UT of day 25. With the 10-sample ensemble average, the storm peak occurred around 08:00 UT of day 25. There was a slight improvement of 1 h with the 50-sample ensemble average, with the peak occurring on 09:00 UT of day 25.

6.6. BR 2386 (Starting 30 May 2008)

[64] Four compressions were forecasted during BR 2386 with one of them being a FA. The first compression was forecasted early but was measured later at ACE. The second density amplification was forecasted later than actually measured by ACE. The third compression was forecasted on time. All three compressions were CIR disturbances.

[65] The first storm had a measured peak of *Dst* −16 nT around 01:00 UT of day 9. As shown in Table 3, this storm peak occurred later at around 05:00 UT for an ensemble of 10 simulated samples. For the 50-sample average, the timing improved to 04:00 UT of day 9.

[66] The compressions accompanying the second storm produced moderate driving with a compressed IMF B_z = −10 nT. The geomagnetic activity caused by this amplification peaked around 08:00 UT of day 16 with a measured peak magnitude of −40 nT. The storm peak occurred around 08:00 UT of day 17 for the 10-sample average. With the 50-sample average, the simulated *Dst* peaked on 11:00 UT of day 17.

[67] The last storm measured in the rotation was around 05:00 UT of day 26 with a peak intensity of −25 nT. This storm occurred on 05:00 UT of day 5 of the next rotation (BR 2387) for the 10 simulated signal samples average. There was not much improvement with the 50-sample average, the storm peak occurred on 08:00 UT of day 5 of BR 2387. As seen in Figure 8, this event (event 13) has a variance of +1 to −1 days around a mean delay time of 5 days.

[68] The first density compression was a FA as seen in Table 2. Again, there was a coronal hole seen in the SOHO images but no disturbance was recorded at ACE.

6.7. BR 2387 (Starting 26 June 2008)

[69] From Table 2, there were two compressions measured in this rotation by ACE.

[70] The first compression was measured later relative to the forecast. During this event, the solar wind speed in the HSS was measured around 700 km/s with an IMF compression of 15 nT. The peak geomagnetic activity was measured on the ground at 09:00 UT of day 16. For the simulated *Dst*, the peak with the 10-sample average was around 23:40 UT of day 15. The same activity peaked around 22:00 UT of day 15 for the 50-sample average.

[71] The compression labeled ME in Table 2 for this rotation was in fact added from the uncalibrated analysis. The relatively stable coronal hole present during the previous Bartel rotations was not visible in the images in this instance, but we added the compression because it was directly correlated with the event. This last storm had a very large density enhancement duration which was reflected in the *Dst* being positive for the same period. The measured negative *Dst* peak time occurred around 01:00 UT of the first day of BR 2388 (the next rotation) with a moderate value of −24 nT as seen in Table 3. With the 10-sample average, the simulated storm

peak time occurred around 03:00 UT of day 26. The timing did not change much for the 50-sample average which gave a storm peak around 04:00 UT of day 26. This is event 15 of Figure 8.

[72] There was also a FA (second compression in Table 2). A coronal hole was seen in the SOHO images but no transients were measured by the ACE satellite.

6.8. BR 2388 (Starting 23 July 2008)

[73] From Table 2, we see three compressions after video calibration. These three compressions are shown in Figure 5. However, only the second compression was an actual CIR event. This indicated that the coronal holes seen in the EIT images were not geoeffective. A fourth compression on the 25th day was a ME according to video calibration. Here, similar to BR 2387, we used knowledge from the uncalibrated analysis to add the compression into the proton density profile.

[74] The first true CIR event on day 17 was forecasted later than was actually measured at ACE. The second true event on day 25 was forecasted on time. This can be seen in Figure 7.

[75] The first storm peak (event 16 in Table 3) was measured on 06:00 UT of day 18 with a peak *Dst* of −40 nT. The peak intensification in geoactivity occurred around 22:00 UT of day 18 for the 10-sample average. The simulated peak for the 50-sample average was recorded around 21:00 UT of day 18. This can be seen in Figure 8, where for event 16, the sample timings are clustered around 12 h after the measured negative *Dst* peak.

[76] The second storm peaked on 15:00 UT of day 26. As seen in Table 3, the peak negative simulated *Dst* derived from WINDMI model occurred around 05:00 UT of day 26 for the 10-sample average. The 50-sample average produced a peak around 03:00 UT of day 26. As seen in Figure 8, this event (event 17) had all the sample timings occurring before the measured *Dst*.

[77] Table 2 shows that the other two events are FAs (days 5 and 21). There was an increase in the measured proton density around the time when these compressions were forecasted (as seen in Figure 7), but they lacked other signatures of CIRs like increase in solar wind speed. This increase was due to heliospheric current sheet (HCS) crossing which we concluded through examining the synoptic map during the time of interest.

6.9. BR 2389 (Starting 19 August 2008)

[78] From Table 2 we observe that two compressions were forecasted and were also measured by ACE with CIR signatures. The first compression was forecasted on time while the second was forecasted much earlier than it was measured at ACE.

[79] The first compression seen in the density plot (Figure 6), was made up of three simultaneous compressions around 03:00 UT, 15:00 UT of day 15, and 00:00 UT of day 16. The IMF compressions that accompanied the plasma compression caused a geomagnetic storm peak of −51 nT on 05:00 UT of day 16. The 10-sample average produced a simulated peak storm time on 10:00 UT of day 16. The 50-sample average produced a storm peak around 12:00 UT of day 16.

[80] The second storm produced moderate driving with an IMF $|B| \approx 13$ nT, HSS speed peaking around 600 km/s, and a proton density compression of 20 particles cm^{-3}. The measured geomagnetic activity peaked on 12:00 UT of the first day of the next rotation (BR 2390). This storm is labeled event 19 in Figure 8. The simulated storm peak occurred around 11:00 UT of day 26 for the 10-sample average. The storm peak occurred around 12:00 UT of day 26 with the 50-sample average.

6.10. BR 2390 (Starting 15 September 2008)

[81] Three coronal holes were seen during this rotation which implied that three compressions were forecasted in the synthetic proton density. Only two compressions were CIRs with the first amplification being a FA. The first CIR compression was forecasted on time while the second compression was forecasted before the actual ACE measurement.

[82] The first compression was a CIR with the solar wind speed inside the HSS peaking to 700 km/s. The measured *Dst* peaked around 13:00 UT of day 17. The storm peak was captured in the simulated *Dst* on 06:00 UT of day 17 for both 10- and 50-sample averages.

[83] The next CIR was the second most geoeffective during the year 2008 in terms of peak negative *Dst* which went to −60 nT on 12:00 UT of day 26. The peak occurred on 09:00 UT of day 26 for the 10 simulated samples average. The same peak occurred half an hour before around 08:30 UT of day 26 for the 50 simulated samples average. This can also be seen in the scatterplot for this event (labeled event 21 in Figure 8) where timings were forecasted consistently before being measured.

[84] The compression on day 7 (Figure 6) was a false alarm (FA), as mentioned in Table 2. Because of a 1.3 year modulation of the compressions, the FA is hardly evident in Figure 6. Since there were no classical CIR signatures like increase in speed after the compression, this event was considered a FA. Synoptic maps during the time showed a current sheet crossing which could be the reason for this density enhancement.

6.11. BR 2391 (Starting 12 October 2008)

[85] As in BR 2388, this rotation also had four coronal holes appearing in the central meridian slice. Two were actual CIRs with the other two being FAs. The first CIR compression was forecasted on time while the second was forecasted before actually measured by ACE.

[86] The first measured storm was fairly weak with a peak negative *Dst* of −24 nT on 07:00 UT of day 17 as indicated by event 22 in Table 3. The peak timing from an average of 10 simulated samples was 17:00 UT of day 17. On the other hand, the same storm peaked at around 15:00 UT of day 17, for the 50-sample average. Note from Table 2 that although the density compression occurred on time, the magnetospheric response simulated by the WINDMI model occurred later because of IMF B_z being a random signal.

[87] The last storm peak in this rotation was measured on 10:00 UT of day 26. This is event 23 shown in Table 3. The storm peaked on 07:00 UT of day 26 with an average of 10 simulated signals. With the 50-sample average the storm peak occurred around 06:55 UT of day 26.

[88] The first two simulated compressions as shown in Figure 6 and Table 2 were false alarms. However, using the synoptic maps, we concluded that the second FA (around day 13) had an increase in measured proton density because of current sheet crossing.

6.12. BR 2392 (Starting 8 November 2008)

[89] Three coronal holes were seen in the EIT images which indicated three density compressions. When the synthetic signal was compared against measured ACE data, all three corresponded well with CIR type signatures. As seen in Table 2, all the three compressions were forecasted either before or on time relative to ACE satellite measurements.

[90] For the first storm, the solar wind conditions as measured by ACE were not very strong, with slow stream speeds around 300 km/s and HSS value around 500 km/s. The first storm measured in the ground *Dst* peaked to a negative maximum of -31 nT around 05:00 UT of day 8. The 10 simulated *Dst* samples average produced a peak around 17:00 UT of day 7. The 50 simulated *Dst* samples average produced a peak on 15:00 UT of day 7.

[91] The second storm was very weakly geoeffective as seen in Table 3 with a peak negative value of -11 nT on 08:00 UT of the day 18. The 10-sample average produced a peak on 14:00 UT of day 18. The 50-sample average produced a peak around 13:00 UT of day 18. This is evident in Figure 8 where this storm is tagged event 25 and had forecasts clustered around 0 (on time) with a variance of -0.3 to $+0.3$ days (-7 to 7 h).

[92] The last compression was a result of the interaction between slow wind (speed around 300 km/s) and HSS (speed around 600 km/s), with a strong compression in the IMF (around 20 nT mainly contributed by IMF B_y). An IMF B_z peak negative magnitude of -13 nT resulted in geomagnetic activity which peaked on 10:00 UT of day 1 of BR 2393. However, the 10 simulated *Dst* samples average produced a peak on 15:00 UT on day 25 of BR 2392. The 50-sample average produced a peak on 16:00 UT of day 25. This feature is evident from Figure 8 where this is event 26.

6.13. BR 2393 (Starting 5 December 2008)

[93] As indicated in Table 2, the first event, termed a missed event, was weakly geoeffective with a peak value in the measured *Dst* of -11 nT. The next two storms were also very weak with peak measured *Dst* of -15 and -14 nT. The compressions related to these CIRs were forecasted before they were actually measured at ACE.

[94] For the ME, no coronal holes could be seen in the central slice of SOHO images and so no compressions and hence no geomagnetic activity was captured in the simulated *Dst*.

[95] The next storm peaked at 00:00 UT of day 19 with a negative *Dst* value of -15 nT as given in Table 3. The 10-sample average produced a peak on 04:00 UT of day 18. The 50 simulated samples average produced the storm peak on 05:00 UT of day 18. This is also evident in Figure 8 where this event, event 27, was consistently forecasted early.

[96] The last CIR event was measured with a peak *Dst* of -14 nT on 07:00 UT of day 26. This storm peak was captured around 19:00 UT of day 26 with the 10-sample average. The event peak was forecasted around 17:00 UT of day 26 with the 50-sample average.

6.14. Events Summary

[97] The above discussion, Table 3, and Figure 8 indicate that the timings obtained from 10- to 50-sample averages were consistent in terms of forecasting the storm before or after its actual occurrence. Both the 10- and 50-sample ensembles show a consistent pattern with regards to the forecast of timing a particular CIR driven storm. The worst case timing forecast for when the storm was measured before it was forecasted was around 3 days (variance of -1 to $+2$ days) later for the last storm in BR 2383 (event 6 in Table 3 and Figure 8), 4 days (with a variance of -1 to $+1$ day) later for the last storm of BR 2386 (event 13 in Table 3 and Figure 8), and 2 days (variance -1 to $+1$ day) later for the first storm in BR 2392 (event 24 in Table 3 and Figure 8). Since the representative samples are averaged, the short-time features are lost, but the main phase peak timings (which is the goal of this study) are roughly preserved. The plots for averages of 10 and 50 representative samples compared to the ground *Dst* are included in the auxiliary material as is the *Dst* output from the WINDMI model for actual ACE flow and IMF parameters.[1] Last, as previously asserted, accurately timing the density enhancement will not guarantee an on time storm peak (e.g., both storms in BR 2381) owing to the random nature of the IMF B_z with southward turning occurring somewhere inside the compression.

7. Conclusions and Future Work

[98] In this work we used SOHO/EIT and STEREO B/EUVI 19.5 nm images, together with ACE solar wind data, to construct a set of synthetic signals of v_x, B_z, N_p as inputs to the WINDMI model. The aim of the study was first to time the CIR event and secondly to generate the expected profiles of solar wind parameters at 1 AU. With a radial velocity assumed at 500 km/s and ballistic propagation from the Sun to 1 AU, we simulated 3.5 day ahead forecasts for these events. We did this during a solar minimum since at other times the presence of bursty events like CMEs or accelerated flows (as in BR 2383) may affect the arrival times of each disturbance.

[99] The density and velocity profiles were adequately represented by Gaussian and sinusoidal variations with the timings being taken from images and the signal construction methods taken in part from previous works. In the case of the IMF B_z, we found that a randomly generated signal was more useful than a periodic signal to account for any prestorm or poststorm B_z fluctuations that might precondition and delay the recovery of the *Dst*. This randomness in B_z produced a distribution of possible *Dst* signatures. We have generated 10 samples of simulated IMF B_z signals and incorporated the corresponding simulated *Dst* forecasts into a movie that is included with the auxiliary material. These different possibilities result in slightly different onset times, and levels of geomagnetic activity.

[100] In future work, we will optimize the parameters in the WINDMI model to predict the ring current characteristic recovery times during a CIR storm. This might vary from storm to storm depending on how far or close the next compression is and the amplitude of B_z in the high-speed stream. Automation of coronal hole detection will be useful for estimating the arrival times. To this end we intend to use image processing techniques to remove the transient

[1]Auxiliary materials are available in the HTML. doi:10.1029/2011JA017018.

dimming. We will also compare the ring current dynamics during the CIR events against strong CME-type events.

[101] **Acknowledgments.** The authors acknowledge the CalTech Web site for ACE data, the NASA Web site for images from SOHO and STEREO, and the Royal Observatory of Belgium for providing the processed images through the Solar Weather Browser (SWB). The authors also acknowledge the CME list provided by the CACTUS software at http://sidc.oma.be/cactus/ and synoptic maps provided on the CCMC STEREO support Web site. M. L. Mays is supported by an appointment to the NASA Postdoctoral Program at the Goddard Space Flight Center, administered by Oak Ridge Associated Universities through a contract with NASA.

[102] Philippa Browning thanks the reviewers for their assistance in evaluating this paper.

References

Burlaga, L. F., K. W. Behannon, S. F. Hansen, G. W. Pneuman, and W. C. Feldman (1978), Sources of magnetic fields in recurrent interplanetary stream, *J. Geophys. Res.*, *83*, 4177–4185, doi:10.1029/JA083iA09p04177.

Carovillano, R. L., and G. L. Siscoe (1969), Corotating structures in the solar wind, *Sol. Phys.*, *8*, 401–414.

Dessler, A., and E. N. Parker (1959), Hydromagnetic theory of geomagnetic storms, *J. Geophys. Res.*, *64*, 2239–2252, doi:10.1029/JZ064i012p02239.

de Toma, G. (2010), Evolution of coronal holes and implications for high-speed solar wind during the minimum between cycles 23 and 24, *Sol. Phys.*, doi:10.1007/s11207-010-9677-2.

Dungey, J. W. (1961), Interplanetary magnetic field and the auroral zones, *Phys. Rev. Lett.*, *6*(2), 47–48.

Edmondson, J. K., S. K. Antiochos, C. R. DeVore, B. J. Lynch, and T. H. Zurbuchen (2010), Interchange reconnection and coronal hole dynamics, *Astrophys. J.*, *714*, 517–531, doi:10.1088/0004-637X/714/1/51.

Gosling, J. T., and V. J. Pizzo (1999), Formation and evolution of corotating interaction regions and their three dimensional structure, *Space Sci. Rev.*, *89*, 21–52.

Hviuzova, T. A., S. V. Tolochkina, and V. L. Zverev (2007), Variations in the IMF vertical component in isolated solar wind streams, *Geomagn. Aeron.*, *47*(2), 149–155, doi:10.1134/S0016793207020028.

Jacobs, J. A., Y. Kato, C. Matsushita, and V. A. Troitskaya (1964), Classification of geomagnetic micropulsations, *J. Geophys. Res.*, *69*, 180–181, doi:10.1029/JZ069i001p00180.

Lee, M. A. (2000), An analytical theory of the morphology, flows, and shock compressions at the corotating interaction regions in the solar wind, *J. Geophys. Res.*, *105*, 10,491–10,500.

Luo, B., Q. Zhong, S. Liu, and J. Gong (2008), A new forecasting index for solar wind velocity based on *eit* 28.4 nm observations, *Sol. Phys.*, *250*, 159–170, doi:10.1007/s11207-008-9198-4.

Mann, I. R., T. P. O'Brien, and D. K. Milling (2004), Correlations between ULF wave power, solar wind speed, and relativistic electron flux in the magnetosphere: Solar cycle dependence, *J. Atmos. Sol. Terr. Phys.*, *66*, 187–198, doi:10.1016/j.jastp.2003.10.002.

McComas, D. J., H. A. Elliott, J. T. Gosling, D. B. Reisenfeld, R. M. Skoug, B. E. Goldstein, M. Neugebauer, and A. Balogh (2002), Ulysses' second fast-latitude scan: Complexity near solar maximum and the reformation of polar coronal holes, *Geophys. Res. Lett.*, *29*(9), 1290, doi:10.1029/2001GL014164.

McGregor, S. L., W. J. Hughes, C. N. Arge, D. Odstrcil, and N. A. Schwadron (2011), The radial evolution of solar wind speeds, *J. Geophys. Res.*, *116*, A03106, doi:10.1029/2010JA016006.

Meredith, N. P., M. Cain, R. Horne, R. M. Thorne, D. Summers, and R. R. Anderson (2003), Evidence for chorus-driven electron acceleration to relativistic energies from a survey of geomagnetically disturbed periods, *J. Geophys. Res.*, *108*(A6), doi:10.1029/2002JA009764.

Nolte, J. T., A. S. Krieger, A. F. Timothy, R. E. Gold, E. C. Roelef, G. Vaina, A. J. Lazarus, J. D. Sullivan, and P. S. McIntosh (1976), Coronal holes as sources of solar wind, *Sol. Phys.*, *46*(2), 303–322, doi:10.1007/BF00149859.

O'Brien, T. P., R. L. McPherron, D. Sornette, G. D. Reeves, R. Friedel, and H. J. Singer (2001), Which magnetic storms produce relativistic electrons at geosynchronous orbit?, *J. Geophys. Res.*, *106*, 15,533–15,544.

Padhye, N. S., C. W. Smith, and W. H. Matthaeus (2001), Distribution of magnetic field components in the solar wind plasma, *J. Geophys. Res.*, *106*, 18,635–18,650, doi:10.1029/2000JA000293.

Patra, S., E. Spencer, W. Horton, and J. Sojka (2011), Study of *Dst*/ring current recovery times using the WINDMI model, *J. Geophys. Res.*, *116*, A02212, doi:10.1029/2010JA015824.

Pizzo, V. J. (1980), A three-dimensional model of corotating streams in the solar wind: 2. Hydrodynamic streams, *J. Geophys. Res.*, *85*, 727–743.

Pizzo, V. J. (1991), The evolution of corotating stream fronts near the ecliptic plane in the inner solar system: 2. Three-dimensional tilted-dipole fronts, *J. Geophys. Res.*, *96*, 5405–5420.

Reiff, P. H., and J. G. Luhmann (1986), Solar wind control of the polar-cap voltage, in *Solar Wind Magnetosphere Coupling*, pp. 453–476, Terra Sci., Dordrecht, Netherlands.

Richardson, I. G., E. W. Cliver, and H. V. Cane (2000), Sources of geomagnetic activity over the solar cycle: Relative importance of coronal mass ejections, high-speed streams, and slow solar wind, *J. Geophys. Res.*, *105*, 18,203–18,213, doi:10.1029/1999JA000400.

Richardson, I. G., et al. (2006), Major geomagnetic storms ($Dst \leq -100$ nt) generated by corotating interaction regions, *J. Geophys. Res.*, *111*, A07S09, doi:10.1029/2005JA011476.

Richardson, J. D., K. I. Paularena, J. W. Belcher, and A. J. Lazaru (1994), Solar wind oscillations with a 1.3 year period, *Geophys. Res. Lett.*, *21*, 1559–1560.

Robbins, S., C. J. Henney, and W. Harvey (2006), Solar wind forecasting with coronal holes, *Sol. Phys.*, *233*, 265–276, doi:10.1007/s11207-006-0064-y.

Robbrecht, E., and D. Berghmans (2004), Automated recognition of coronal mass ejections (CMEs) in near-real-time data, *Astron. Astrophys.*, *425*(3), 1097–1106, doi:10.1051/0004-6361:20041302.

Schwenn, R. (1990), Large-scale structure of the interplanetary medium, in *Physics of the Inner Heliosphere*, vol. 1, *Phys. Chem. Space*, vol. 20, pp. 99–181, Springer, Berlin.

Sckopke, N. (1966), A general relation between the energy of trapped particles and the disturbance field near the Earth, *J. Geophys. Res.*, *71*, 3125–3130, doi:10.1029/JZ071i013p03125.

Sheeley, N. R., J. R. Asbridge, S. J. Bame, and J. W. Harvey (1977), A pictoral comparison of interplanetary magnetic field polarity, solar wind speed, and geomagnetic disturbance index during the sunspot cycle, *Sol. Phys.*, *52*, 485–495.

Siscoe, G. L., and L. T. Finley (1970), Solar wind structure determined by corotating coronal inhomogeneities: 1. Velocity driven perturbations, *J. Geophys. Res.*, *75*, 1817–1825.

Siscoe, G. L., and L. T. Finley (1972), Solar wind structure determined by corotating coronal inhomogeneities: 2. Arbitrary perturbations, *J. Geophys. Res.*, *77*, 35–45.

Spencer, E., W. Horton, L. Mays, I. Doxas, and J. Kozyra (2007), Analysis of the 3–7 October 2000 and 15–24 April 2002 geomagnetic storms with an optimized nonlinear dynamical model, *J. Geophys. Res.*, *112*, A04S90, doi:10.1029/2006JA012019.

Tsurutani, B. T., W. D. Gonzalez, A. L. C. Gonzalez, F. Tang, J. K. Arballo, and M. Okada (1995), Interplanetary origin of geomagnetic activity in the declining phase of the solar cycle, *J. Geophys. Res.*, *100*, 21,717–21,733, doi:10.1029/95JA01476.

Tsurutani, B. T., B. Dasgupta, C. Galvan, M. Neugebauer, G. S. Lakhina, J. K. Arballo, D. Winterhalter, B. E. Goldstein, and B. Buti (2002), Phase-steepened Alfvén waves, proton perpendicular energization and the creation of magnetic holes and magnetic decreases: The ponderomotive force, *Geophys. Res. Lett.*, *29*(24), 2233, doi:10.1029/2002GL015652.

Turner, J. M., L. F. Burlaga, N. F. Ness, and J. F. Lemaire (1977), Magnetic holes in the solar wind, *J. Geophys. Res.*, *82*, 1921–1924.

Turner, N. E., E. J. Mitchell, D. J. Knipp, and B. A. Emery (2006), Energetics of magnetic storms driven by corotating interaction regions: A study of geoeffectiveness, in *Recurrent Magnetic Storms: Corotating Solar Wind Streams*, *Geophys. Monogr. Ser.*, vol. 167, edited by B. Tsurutani et al., pp. 113–124, AGU, Washington, D. C.

Vrsnak, B., M. Temmer, and A. M. Veroni (2007a), Coronal holes and solar wind high-speed streams: I. Forecasting the solar wind parameters, *Sol. Phys.*, *240*, 315–330, doi:10.1007/s11207-007-0285-8.

Vrsnak, B., M. Temmer, and A. M. Veroni (2007b), Coronal holes and solar wind high-speed streams: II. Forecasting the geomagnetic effects, *Sol. Phys.*, *240*, 331–346, doi:10.1007/s11207-007-0311-x.

Wood, B. E., R. A. Howard, A. Thernisien, and D. G. Socker (2010), The three-dimensional morphology of a corotating interaction region in the inner heliosphere, *Astrophys. J. Lett.*, *708*, L89–L94.

Zhang, Y., W. Sun, X. S. Feng, C. S. Deehr, C. D. Fry, and M. Dryer (2008), Statistical analysis of corotating interaction regions and their geoeffectiveness during solar cycle 23, *J. Geophys. Res.*, *113*, A08106, doi:10.1029/2008JA013095.

Zurbuchen, T. H., and I. G. Richardson (2006), In-situ solar wind and field signatures of interplanetary coronal mass ejections, *Space Sci. Rev.*, *123*(1–3), 31–43, doi:10.1007/s11214-006-9010-4.

T. Andriyas, A. Raj, and E. Spencer, Center for Space Engineering, Utah State University, Logan, UT 84322, USA. (tushar.andriyas@aggiemail.usu.edu)

M. L. Mays, NASA Goddard Space Flight Center, Greenbelt, MD 20771, USA.

J. Sojka, Center for Atmospheric and Space Sciences, Utah State University, 4405 Old Main Hill, SER Bldg., Rm. 246, Logan, UT 84322-4405, USA.